An Assessment of Differences in ENSO Mechanisms in a Coupled GCM Simulation

Francisco Alvarez-Garcia, William Cabos Narvaez, and Maria J. Ortiz Bevia

Departamento de Física, Universidad de Alcalá, Acalá de Henares, Spain

ABSTRACT

This study investigates the physical mechanisms involved in the generation and decay of El Niño–Southern Oscillation episodes in a coupled GCM simulation. Warm and cold events found in a 100-yr-long record are separated into groups by means of a clustering technique that objectively discriminates common features in the evolution of the tropical Pacific heat content anomalies leading to the event's peak. Through an analysis of the composites obtained from this classification, insight is gained as to the processes responsible for the presence of different behaviors. Three classes of warm events were identified. The first is characterized by the westward propagation of warm heat content anomalies north of the equator before the onset of the episode. This propagation characteristic of the delayed oscillator paradigm appears weakened in the decay of the episode. In the second class, local development of heat content anomalies in the northwest tropical Pacific, associated with overlying wind stress curl anomalies, dominates both the generation and the decay of the warm event. In addition, subsurface cold anomalies form in the equatorial western Pacific in association with the poleward flow considered by the recharge–discharge oscillator model. The third class is characterized by a relatively quick development of the warm episode. Attention is focused on the first two classes. The suitability of different conceptual models to explain them is addressed. Previous analyses of the simulation are reviewed throughout this work. Differences between the classes are related to a regime shift that occurs toward the middle of the record.

1. Introduction

The mechanisms that drive the tropical Pacific atmosphere–ocean system from one phase of El Niño–Southern Oscillation (ENSO) to the other have become one of the main topics of research in the field. Recognition of the coupled instabilities that are responsible for the growth of ENSO episodes dates back to the ideas of Bjerknes (1969), while the so-called transition mechanism is still not well agreed upon. This knowledge is relevant for issues such as the debate concerning the apparent oscillatory nature of ENSO, or the effective potential for its predictability (Kessler 2002).

Previous studies have proposed a number of conceptual paradigms for ENSO. Each of these paradigms selects a physical mechanism that can produce the characteristic interannual oscillations in the tropical Pacific atmosphere–ocean system.

Ocean wave dynamics act as a key factor in the de-

layed oscillator model: during an ENSO event, wind stress anomalies over the central equatorial Pacific trigger westward-traveling oceanic Rossby waves; these reflect back at the western boundary as eastward-propagating Kelvin waves. The arrival of the Kelvin wave signal into the eastern equatorial Pacific opposes the growth of the developing episode and eventually causes the ENSO phase turnabout (Suarez and Schopf 1988; Battisti and Hirst 1989).

The effects of ocean wave propagation are integrated (and thus not explicitly considered) in the quasi-Sverdrup balance postulated by the recharge–discharge conceptual model (Jin 1997). Whereas the equatorial thermocline slope evolves in permanent equilibrium with wind stress anomalies, its zonal mean depth undergoes a slow adjustment process by means of meridional mass exchanges. During a warm ENSO event, poleward flows discharge heat away from the equator, elevating the equatorial zonal mean thermocline and settling favorable conditions for the occurrence of an ensuing cold event. As the latter proceeds, the inverse mechanism of recharge takes place. The recharge–discharge model includes the delayed oscillator as a particular case, and is encompassed in turn in the *sub-*

Corresponding author address: Dr. Francisco Alvarez-Garcia, Departamento de Física, Universidad de Alcala, 28871 Alcala de Henares, Madrid, Spain.
E-mail: franciscoj.alvarez@uah.es

surface memory paradigm (Neelin et al. 1998), alluding to the preponderant role of thermocline dynamics in those two conceptual models.

Wave propagation becomes once more explicit in the western Pacific oscillator model of ENSO (Weisberg and Wang 1997). At the eastern equatorial Pacific, Kelvin waves again provide the negative feedback that brings about the phase change; but, contrary to the delayed oscillator model, their presence is not attributed to Rossby wave reflection. They can arise from zonal wind anomalies generated over the far western equatorial Pacific at the mature stage of an ENSO event: anomalous Ekman pumping induces off-equatorial SST anomalies that in turn give rise to sea level pressure (SLP) anomalies in the overlying atmosphere. It is these SLP anomalies that produce the zonal wind anomalies over the far western Pacific.

The previously overlooked zonal advection of SST and wave reflection at the eastern boundary stand out as fundamental features in the advective–reflective oscillator of Picaut et al. (1997). Driven by either the local or the remotely forced effect of wind stress anomalies, the eastern edge of the warm pool moves away from its mean location during an ENSO episode. Zonal current anomalies stemming from the reflection of oceanic waves in the American coast, together with the annual variations of the mean zonal flow, counteract this displacement and finally change its sign. The associated SST anomalies activate the positive wind stress–SST feedback loop, and thus the oscillation enters into its opposite phase.

The observed variability most likely includes features from all the paradigms above. Under this premise, Wang (2001) attempts to merge the previous mechanisms into a unified ENSO oscillator, formulated as a set of simple ordinary differential equations that reduce to the known models for particular choices of the parameters.

The investigation of the problem cannot remain, however, within the bounds of simple models. More complex physics must be taken into account in order to determine the contribution of distinct processes, the conditions that trigger them, and their possible connections. With an expanding but still limited observational record, coupled general circulation models (CGCMs) emerge as a source of extensive information on the physics of the climate system. Analyses of CGCM simulations can thus improve our comprehension of the mechanisms operating in climate fluctuations with a realistic degree of complexity, and collaterally help to sustain the improvement of CGCMs themselves.

In this work, we investigate the ENSO-like variability found in a state-of-the-art CGCM simulation. By means of a clustering technique, we identify the main characteristics of simulated ENSO episodes and examine how they relate to the different ENSO paradigms described above. Therefore, we restrict our analysis to those elements that characterize the interannual dynamics central to ENSO. Though we are aware that a complete view of ENSO requires examination of its connections with decadal, seasonal, and intraseasonal variability, these aspects are only briefly considered here, as they surpass the limits of our analysis. This is particularly so with regards to the impact of high-frequency variability on ENSO, a problem for which neither our monthly data nor our methodology are well suited.

The tropical Pacific interannual variability in the simulation we analyze here was the object of a previous investigation by Guilyardi et al. (2003, hereafter G03), who focused as well on the mechanisms for ENSO phase change and therefore afforded an essential reference to our work. By adopting a different perspective, we are able to add to their results.

The remainder of the paper includes a description of the analyzed simulation and the data in section 2. We give a brief outline of the methodology in section 3, later expanded in the appendix. Section 4 presents our results, which we summarize and discuss in section 5.

2. Data

The Scale Interaction Experiment (SINTEX) model, as referred to by G03, originated from the European Union (EU) project of the same name, with the coupling of the fourth version of the European Centre Hamburg Atmospheric Model (ECHAM4) atmospheric model and the ORCA oceanic model through the Ocean–Atmoshpere–Sea Ice–Soil (OASIS) interface.

The ECHAM4 is a spectral model that integrates the primitive equations. In the simulation we analyze here, it takes a triangular truncation at wavenumber 30 (T30), equivalent to a 3.75° × 3.75° horizontal resolution. It uses a pressure-based vertical coordinate with 14 irregularly spaced levels between 1000 and 10 hPa. For a detailed description of the AGCM and its performance the reader is referred to Röckner et al. (1996).

The ORCA model (Madec et al. 1998) constitutes the global version of the Océan Parallélisé (OPA8.1), the ocean GCM (OGCM) developed at the Laboratoire d'Océanographic Dynamique et de Climatologie (LODYC). A finite-difference formulation of the primitive equations and of a nonlinear equation of state is given on an Arakawa C grid. The horizontal resolution roughly corresponds to 2° latitude × 1.5° longi-
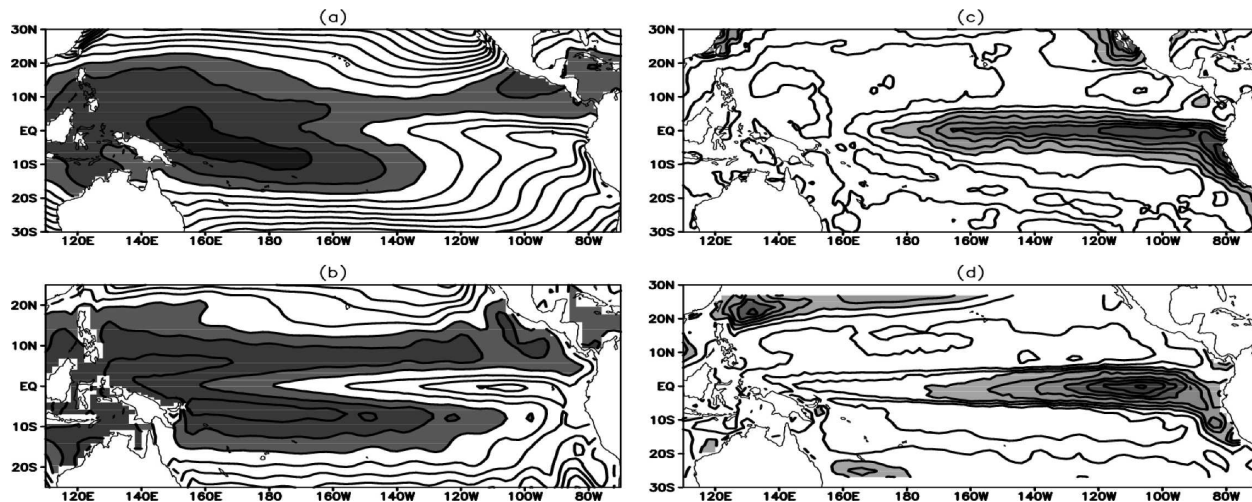
FIG. 1. SST mean conditions in (a) HadISST 1881–1999; (b) SINTEX simulation, years 101–200. Contour interval is 1°C, shaded above 27°C. SST standard deviation in (c) HadISST 1881–1999 and (d) SINTEX simulation, years 101–200. Contour interval is 0.1°C, shaded above 0.6°C.

tude, the latter enhanced to 0.5° near the equator. The model has 31 depth levels, with 10 of them within the upper 100 m of the ocean. Other details include an explicit treatment of the mixed layer that affords minimum diffusion at the thermocline (Blanke and Delecluse 1993).

The OASIS coupler, version 2.4 (Valcke et al. 2000), transfers the necessary information between both elements of the CGCM. The simulation proceeds without any flux adjustment, but for the restoring of sea ice cover to its climatology during the whole simulation, and the use of the *robust diagnostic* technique (Sarmiento and Bryan 1982) in the initialization of ocean currents for 2 yr.

The total length of the SINTEX simulation, as we shall subsequently name it, is 200 yr. Our analysis concentrates on the second half of the record, in order to avoid the subsurface trend of the first 100 yr. Its features, as far as concerns the validation of the tropical Pacific variability, do not differ essentially from the remarks of G03 and of Gualdi et al. (2003) on the complete 200-yr period. In the following, all results and comments, unless stated otherwise, refer to the last 100 yr of the coupled run. Monthly anomalies are computed with respect to the climatology of that interval.

Figure 1 compares SST mean conditions and variance in the SINTEX simulation and in the Hadley Centre Sea Ice and Sea Surface Temperature (HadISST; Rayner et al. 2000) 1881–1999 dataset. Overall, the simulated mean pattern agrees well with observations, though some CGCM typical biases appear, like the too warm SSTs in the southeastern tropical Pacific (Mechoso et al. 1995; Meehl et al. 2001). The problem aggravates

in boreal spring and apparently associates with the deformation of the South Pacific convergenze zone (SPCZ) into a spurious southern ITCZ (Gualdi et al. 2003). On the other hand, SSTs along most of the equator fall below observed values by 1°–2°C. Temperatures rise quickly in the poleward direction, and so yield a too narrow equatorial cold tongue that extends too far west, again a common problem in CGCM experiments (Latif et al. 2001; Meehl et al. 2001) and consistent in the SINTEX run with an overestimation of the easterlies along the equator. Nevertheless, the model provides a good representation of crucial elements, such as a correct zonal SST gradient along the equator and a realistic equatorial thermocline (Gualdi et al. 2003).

The spatial distribution of simulated SST variance closely resembles its observed counterpart (Figs. 1c,d), with the core of maximum variance properly located at the eastern equatorial Pacific and with realistic levels of variance. Underestimation of SST variance, however, can be appreciated in the central equatorial Pacific.

The modal distribution of SST variance is also realistic. An EOF analysis of the tropical Pacific monthly SST anomalies yields a leading mode with a pattern like that in Fig. 1c and with a characteristic time scale of about 2.5 yr, which is shorter than the observed ENSO period range. Explained variance is 40% of the total for this leading mode, and less than 10% for the second one. As to the associated atmospheric variability, the tropical Pacific SLP anomaly–Niño-3 correlation map in Fig. 2 qualitatively depicts the classical seesaw pattern of the Southern Oscillation, with the centers of action displaced equatorward from their observed locations. A dominant ENSO-like mode prevails in the
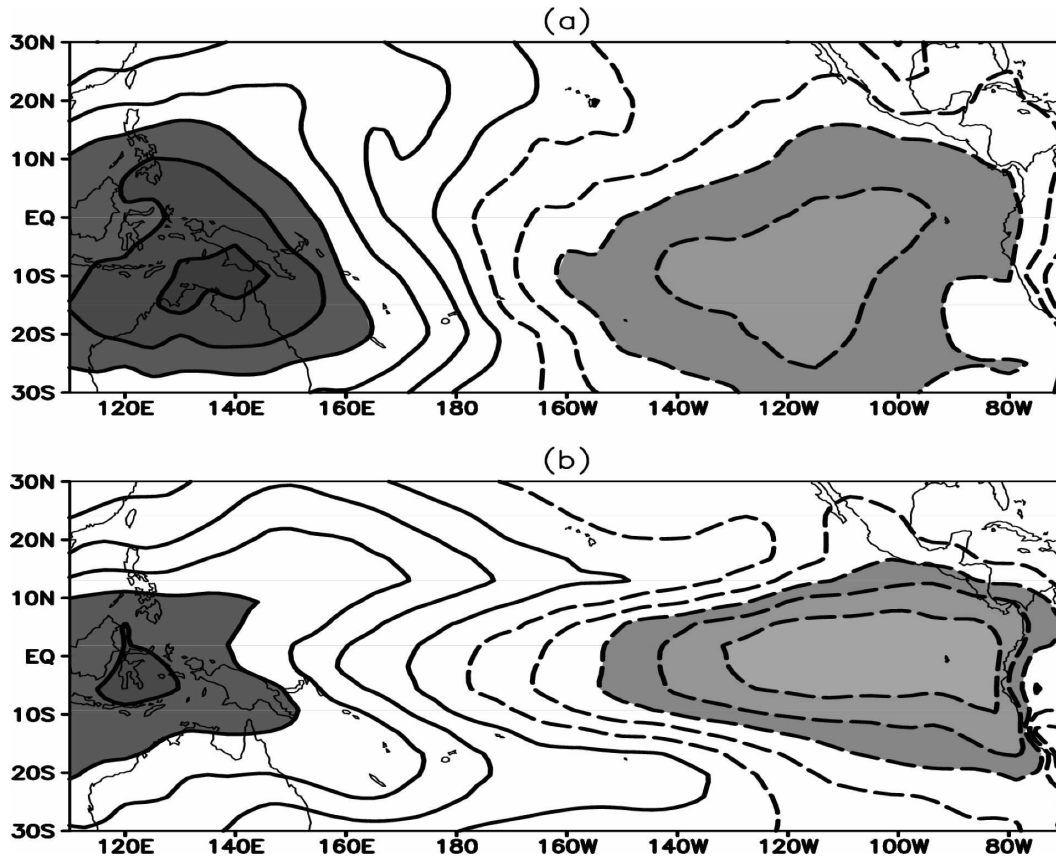
FIG. 2. Tropical Pacific SLP anomaly and Niño-3 index correlation map for (a) GMSLP-HadISST1 and (b) the SINTEX simulation. Contour interval is 0.1, shaded above 0.3.

variability of the tropical Pacific in the SINTEX simulation.

Concerning the intraseasonal variability, the amplitude of the simulated Madden–Julian oscillation (MJO) is realistic albeit it does not propagate as far east as in the ECHAM4 (Sperber et al. 2004).

3. Methodology

This study addresses the causes for the variety of ENSO episodes in the SINTEX simulation. We introduce a procedure capable of detecting classes of events (groups that share a distinct evolution). The final product of such a procedure is a composite event representative of the class behavior.

Composites have been frequently applied to the analysis of ENSO: a recent example is the work of Harrison and Larkin (1998), who update and improve Rasmusson and Carpenter (1982). Another one is G03, devoted to the analysis of the SINTEX run. In these works, events are basically grouped by their peaking in the same season. Other authors have employed differ-

ent criteria in order to group ENSO events, such as, for instance, the amplitude of the SST anomalies in the eastern equatorial Pacific at the peak stage (Yukimoto and Kitamura 2003), or the duration of the episode (Boo et al. 2004). To our knowledge, a method that compares the anomaly fields during the development of different events, and groups these on the basis of an objectively computed measure of distance, was lacking in the current literature on ENSO. Our approach offers this alternate perspective, and seeks for common patterns in the development of different episodes. Thus, it does not attend only to their seasonality, amplitude, duration, or any other simple condition. It is also designed so as to capture the peculiarities of the ENSO episodes that are likely to be blurred by linear statistics tools such as empirical orthogonal functions.

The first step in our methodology requires the identification of the ENSO events occurring in the 100-yr record of the SINTEX simulation. We have employed the Niño-3 time series (SST average anomaly over 5°S–5°N, 150°–90°W) for this purpose. We consider an ENSO episode occurring when the index rises over the

one standard deviation threshold for at least three consecutive months. As an additional condition, we check that the event thus defined is coincidental with extremes in the first principal component of the tropical Pacific SST anomalies and in the atmospheric part of the phenomenon, as represented by a model-adapted version of the Southern Oscillation index (SOI) SLP anomaly index (i.e., the difference between averaged SLP anomaly over 20°–10°S, 125°–135°E and 15°–5°S, 155°–145°W). Our selection practically yields the same result as with the G03 criterion (i.e., it peaks over the 1.5 standard deviations threshold).

a. Classification

For each event, we consider a 16-month segment that ends with the peak anomaly in the Niño-3 index. The choice of this length owes to the characteristic 31-month period dominating the power spectrum of the simulated Niño-3 series. We monitor the event's development in the evolution of the heat content (HC) anomalies in the Pacific basin within 15°S–15°N. To compare different episodes, we compute a distance defined from the spatial correlation between their HC anomaly patterns in each of those 16 months. This distance serves as the basis for our classification, which is carried out by means of a two-step clustering technique. The procedure is repeated with an alternate definition of distance, in order to test the robustness of the classification. More details on this methodology are given in the appendix.

b. Composite significance

An important issue in composite analysis refers to the selection of its significant features. We apply two significance tests: one on the group mean (Terray et al. 2003) and the other on the t values (Brown and Hall 1999). This second method makes use of robust estimators of the location (median) and dispersion (interquartilic range) of the elements within a group that allows us to ensure we only retain those features that consistently appear throughout the class. In the following we comment only on features that pass both these tests at a 95% level.

It is important to note that all (monthly) anomalies are normalized by their corresponding monthly standard deviation prior to the classification process. We must take this step in order to adequately compare episodes with different timing.

4. Results

We found 23 warm events and 19 cold ones in the 100-yr record we analyzed. We categorize the warm episodes into three classes: types W1, W2, and W3, respectively including seven, eight, and five elements; three warm episodes are not assigned to any group by our method. Cold events are also distributed into three classes: types C1 (nine elements), C2 (five elements), and C3 (five elements).

Figure 3 illustrates how classes W1, W2, and W3 are separated in our classification scheme. Figure 3a represents classes W1 and W2 in terms of the distances (see the appendix) to their respective composites or *centroids*. The seven elements in class W1 locate in the upper-left quadrant of the graph, as they are characterized by distances to composite W1 (in the horizontal axis) below a certain threshold, and simultaneously surpass the threshold distance to composite W2 (in the vertical axis). A similar account holds for Figs. 3b,c, so a proper discrimination of the three classes seems to be achieved with this method. The same arguments apply to the classification of cold events.

We will use the equatorial HC (normalized) anomalies time–longitude diagrams of Fig. 4 for a short preliminary description of the composites. Regarding warm composites, type W3 differs from W1 and W2 for its comparative brevity. Its composite shows no sign of the event's development until some 7 months ahead of its peak (month 0). On the contrary, type W1 displays cold conditions in the eastern and central equatorial Pacific more than 1 yr in advance of the event's peak. Warm anomalies accumulate in the west Pacific during this cold phase. The last feature also appears in composite W2, though cold anomalies are absent in the east. From now on, we will leave type W3 out of the discussion because of its comparatively irregular behavior.

Turning to the cold episodes, only class C1 occurs after previous warm anomalies in the eastern Pacific, as shown in Fig. 4. Thus, a distinction between the more regular evolution of composite C1 and the quick growth of types C2 and C3 can also be made for the cold events. Like before, we limit our analysis to this "regular" type C1.

In the following paragraphs, we are concerned with three main questions: 1) what is the source for the warm anomalies preceding the growth of events W1 and W2; 2) what are the negative feedbacks that act in the decay of events W1 and W2; and 3) the same questions as they apply to composite C1.

a. The origin of warm anomalies in composites W1 and W2

Consistent with previous studies (B. Wang et al. 1999) and the study of G03, the northwest tropical Pacific provides, in both W1 and W2, the reservoir of HC
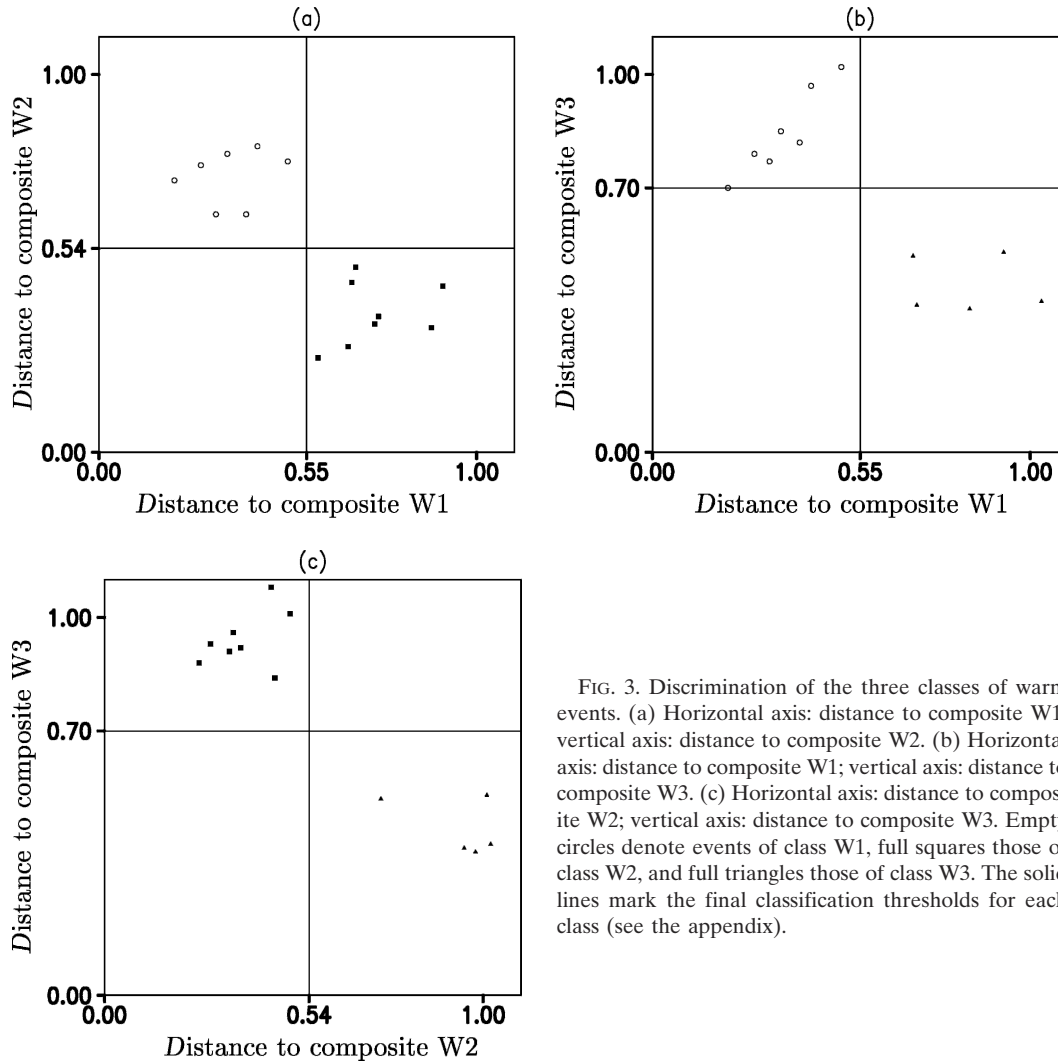
FIG. 3. Discrimination of the three classes of warm events. (a) Horizontal axis: distance to composite W1; vertical axis: distance to composite W2. (b) Horizontal axis: distance to composite W1; vertical axis: distance to composite W3. (c) Horizontal axis: distance to composite W2; vertical axis: distance to composite W3. Empty circles denote events of class W1, full squares those of class W2, and full triangles those of class W3. The solid lines mark the final classification thresholds for each class (see the appendix).

anomalies that will eventually lead to the equatorial warming. Figure 5 compares their evolution in the north tropical Pacific 17–11 months ahead of the Niño-3 peak. Following G03, 6-month-accumulated wind stress curl (WSC6) and HC anomalies are depicted.

Joint westward propagation of HC and WSC6 anomalies characterizes composite W1 (the left column in Fig. 5). Rossby wave activity connected to the preceding ENSO cold phase appears to accumulate heat in the western tropical Pacific, fitting in the delayed oscillator scheme. In fact, the sequence in the left column in Fig. 5 closely resembles the evolution remarked by White et al. (2003) in observations.

In contrast to the former behavior, composite W2 displays a stationary growth of Ekman-pumping-induced HC anomalies, as is shown in the right column in Fig. 5. This local development of northwest Pacific HC anomalies agrees with G03's ENSO composite and

leads them to stress the importance of local Ekman pumping relative to Rossby wave propagation in the SINTEX run. Our results, though, indicate that wave propagation is not so secondary an element in the ENSO physics of the simulation as suggested by G03. It may be inferred from our classification that those two mechanisms tend to operate separately and thus contribute to define distinct groups of ENSO episodes in the simulation.

b. Negative feedbacks in composites W1 and W2

A vertical section of ocean temperature anomalies along the equator at and inmediately after the event's peak (not shown) displays initially, for both composites W1 and W2, the well-known anomalous west–east tilt of the thermocline. It appears in response to the westerly wind anomalies, which have been active for several
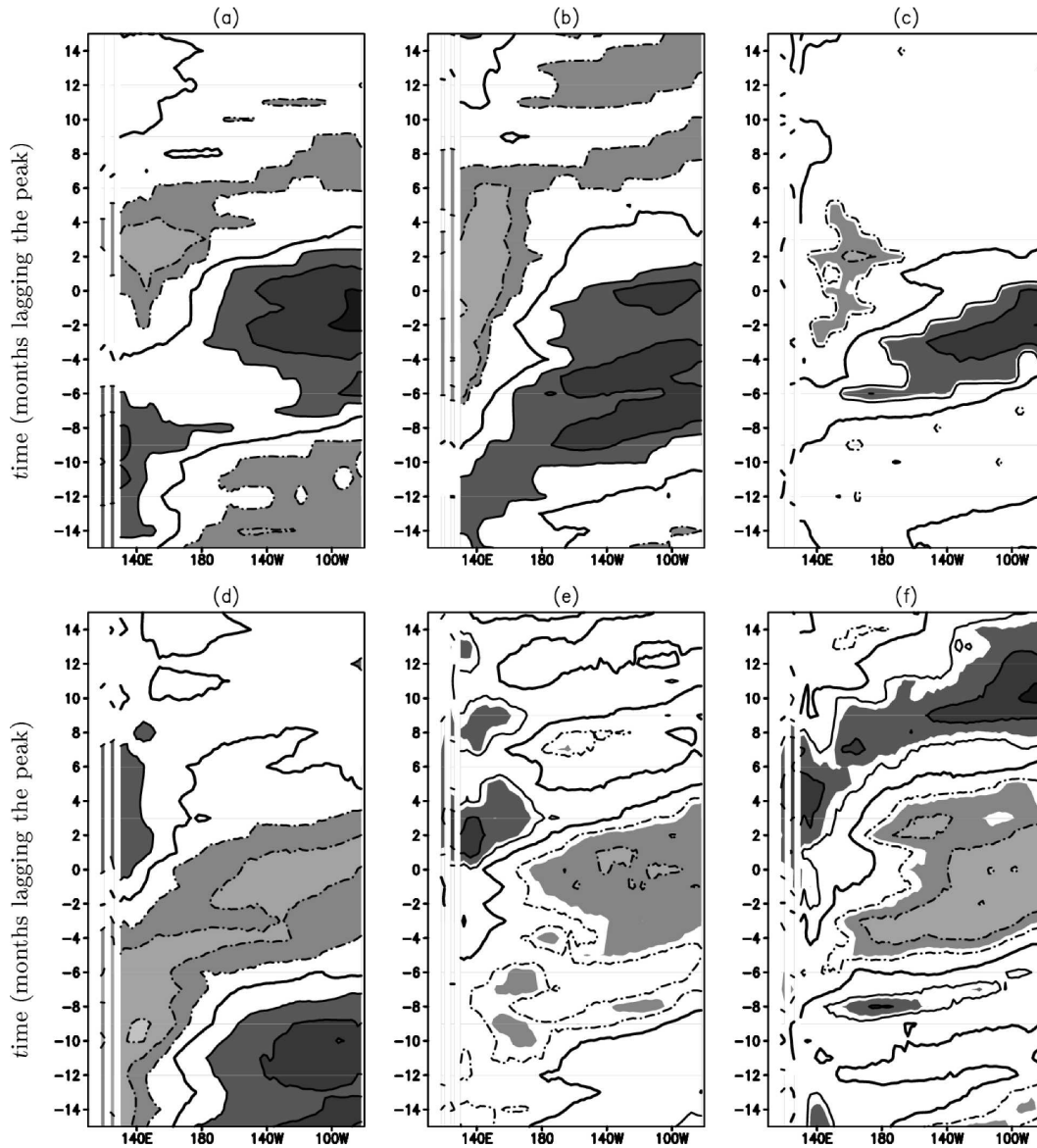
FIG. 4. Time–longitude diagrams of normalized HC anomalies along the equator: class (a) W1, (b) W2, (c) W3, (d) C1, (e) C2, and (f) C3. Contour interval is 0.6, with zero or positive values in solid line. Absolute values over 0.6 are shaded [over 0.8 in (c), (e) and (f)].

months over the central equatorial Pacific. While warm anomalies spread over the upper levels of the eastern to central parts of the basin, subsurface (100–200-m depth) cold anomalies grow in the western equatorial Pacific. A cooling trend then extends eastward at the thermocline depth and progressively erodes the eastern Pacific warm anomalies. This sequential chain of events is consistent with the interpretation of Mantua and Battisti (1994) of the delayed oscillator paradigm. It takes part in the demise of the warm episode in class W1 as well as in W2. Some relevant differences arise, though, from a closer inspection of the composites.

As the event approaches its peak (Fig. 6) local development of cold HC anomalies in association with WSC6 anomalies is conspicuous in composite W2, whereas composite W1 rather shows some faint traces of westward propagation of cold HC anomalies north of the equator. The differences between classes W1 and W2 regarding the evolution of off-equatorial HC anomalies are highlighted in Fig. 7. The HC anomalies averaged over the 5°–10°N band are characterized by westward propagation in composite W1, in contrast with the stationary behavior of composite W2. As stated before, this stationary fluctuation of composite
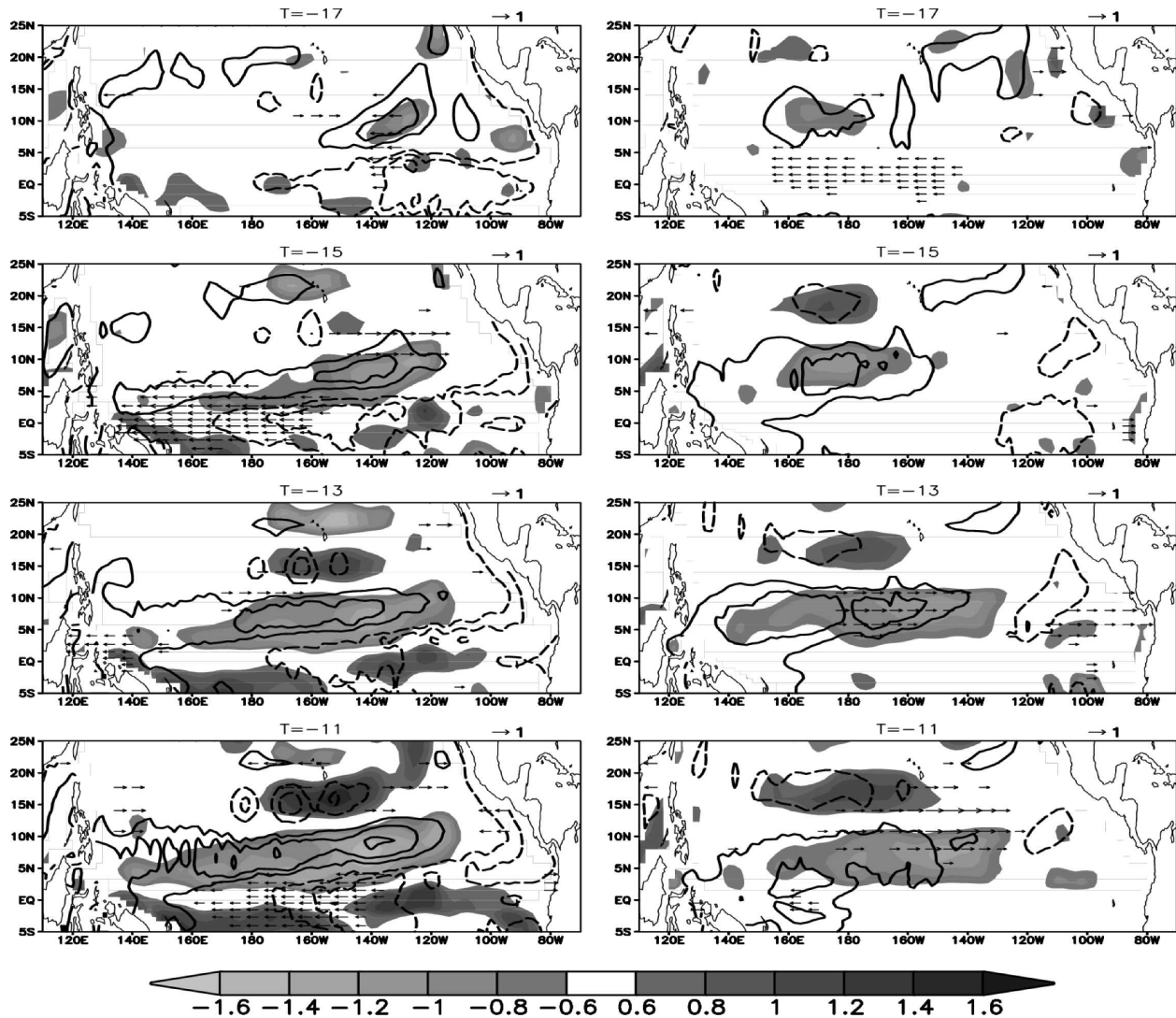
FIG. 5. Evolution of HC and WSC6 anomalies in the north tropical Pacific during months −17 to −11 of composite (left) W1 and (right) W2. Contours: normalized HC anomalies; contour interval is 0.4, only absolute values over 0.6 are depicted; solid (dashed) line indicates positive (negative) values. Shaded: normalized WSC6 anomalies.

W2 agrees with the features of the ENSO composite of G03. In their study, they relate the WSC6 anomalies over the northwest tropical Pacific to the steady Gill response of the atmosphere to the equatorial warming. The comparison of SST anomalies along the equator in types W1 and W2 (Fig. 8) suggests that extensive and persistent warm anomalies, like those of class W2, might be required to induce the WSC6 response in the northwest tropical Pacific.

Persistence and extension of the equatorial SST anomalies also condition the negative feedbacks that contribute to ENSO decay in both composites W1 and W2. Figure 9 illustrates how they differ in the 6-month-accumulated meridional current anomalies, averaged over the 110–140-m layer, at the latitude 1°N. A significant poleward flow, practically absent in W1, characterizes composite W2 and cooperates in the rise of the equatorial thermocline in the western half of the basin. From the vantage point of the recharge–discharge oscillator conceptual model, sustained forcing on the equatorial Pacific by wind stress anomalies leads to the establishment of this flow, geostrophically linked to the thermocline slope adjustment to the anomalous winds. Less prolonged wind forcing in composite W1 would prevent this process from amounting to a significant contribution. It may be noted, however, that the lagged relationship between zonal mean thermocline depth and eastern equatorial SST at the core of the recharge–
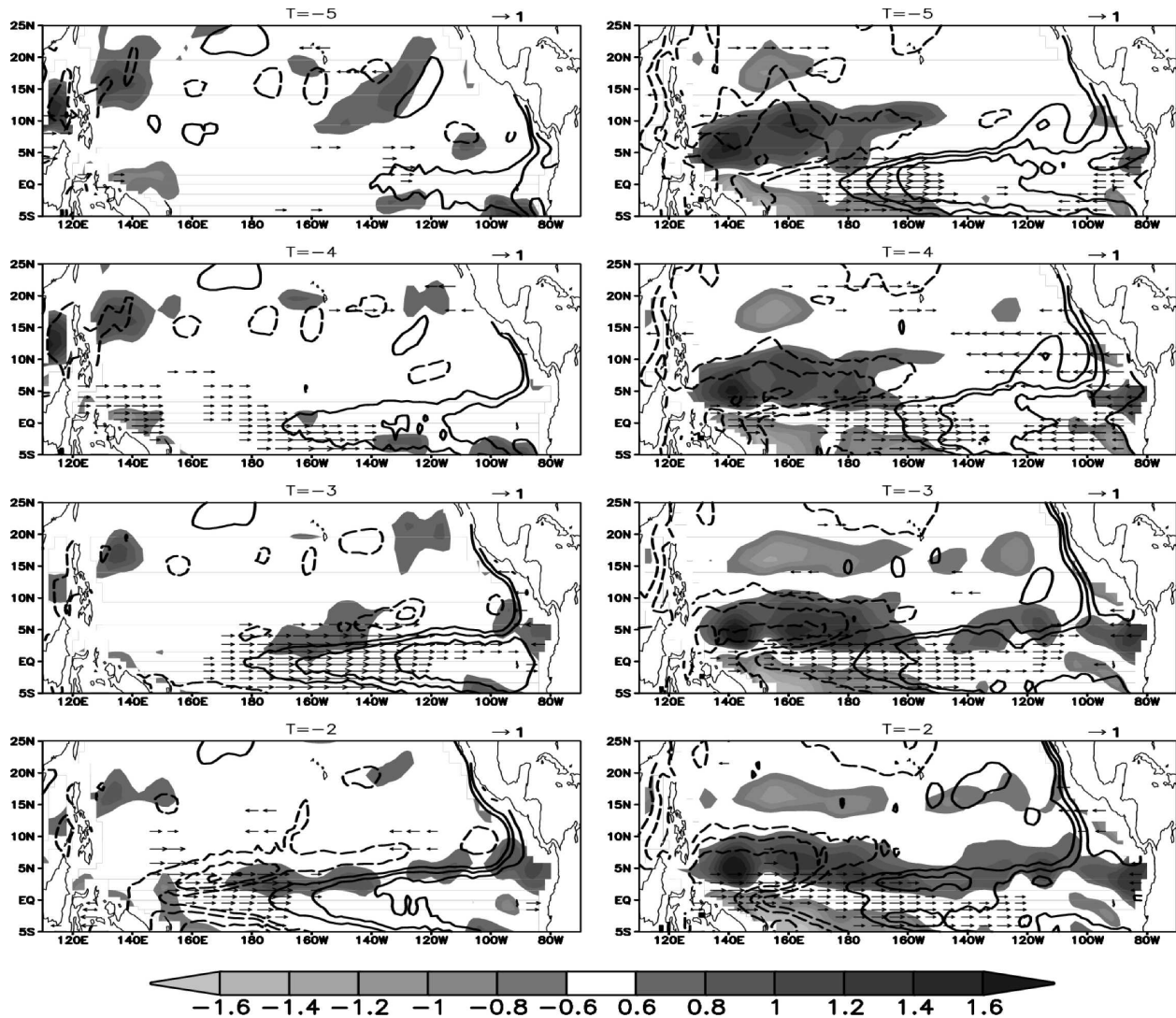
FIG. 6. Same as in Fig. 5, but during months −5 to −2.

discharge oscillator holds for both W1 and W2 classes (Fig. 10).

Differences in the atmospheric response of types W1 and W2 include an interesting feature in the far western Pacific, a key region within the scheme of the western Pacific oscillator (Weisberg and Wang 1997). Zonal wind stress anomalies there can be monitored by means of the Niño-5 index, obtained as the average anomaly over the area 5°S–5°N, 120°–140°E (Wang et al. 1999). When computed for composites W1 and W2 (Fig. 11), this index reveals significant easterly anomalies over the far western Pacific at the mature stage of W1. In contrast, they remain well below the significance threshold in composite W2. Since westerly anomalies tend to occur west of the equatorial SST anomalies, and there are significant SST anomalies west of the date line

for several months in this composite, we think the strong equatorial warming may prevent the appearance of the easterlies over the far western Pacific.

The Niño-5 zonal wind stress anomalies of composite W1 concur with a set of extraequatorial features in the western tropical Pacific. Positive SLP anomalies lie over cold SST anomalies around 10°N and west of 160°E (Fig. 12), describing a pattern highly consistent with the observations of Weisberg and Wang (1997) that inspired the western Pacific oscillator paradigm: the cooling of the sea surface effects the rise in the SLP, which in turn produces the Niño-5 wind anomalies. The cold SST anomalies do not seem to stem from previous wind-induced changes in the upwelling and thermocline depth, as was suggested by Wang et al. (1999). In a latitude–depth cross section (Fig. 13) along 150°E taken
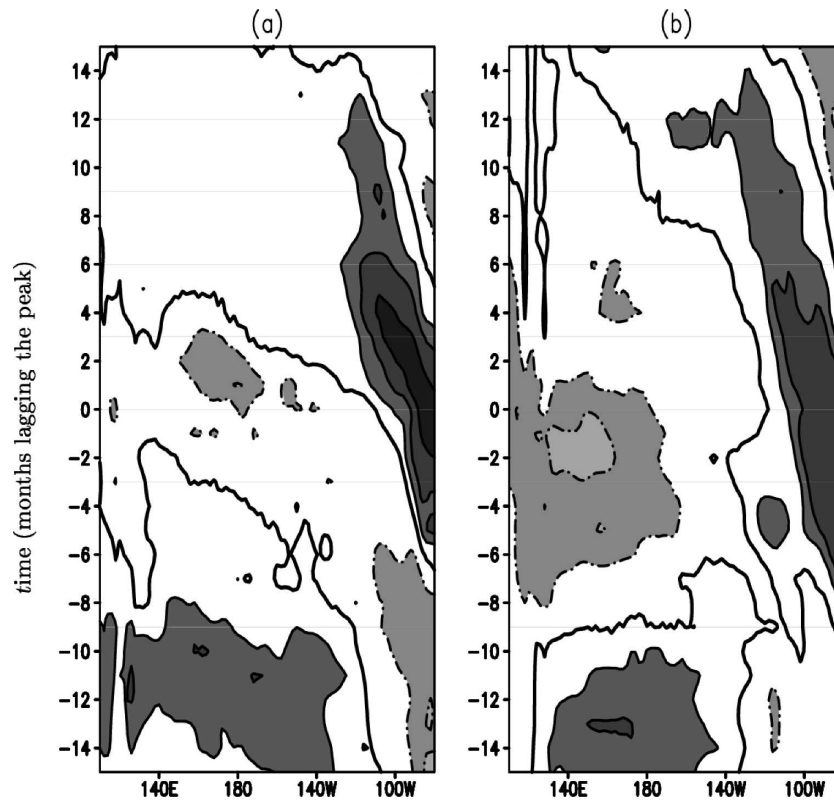
FIG. 7. Time–longitude diagrams of normalized HC anomalies averaged over 5°–10°N: class (a) W1 and (b) W2. Contour interval is 0.6, with zero or positive values in solid line. Absolute values over 0.6 are shaded.
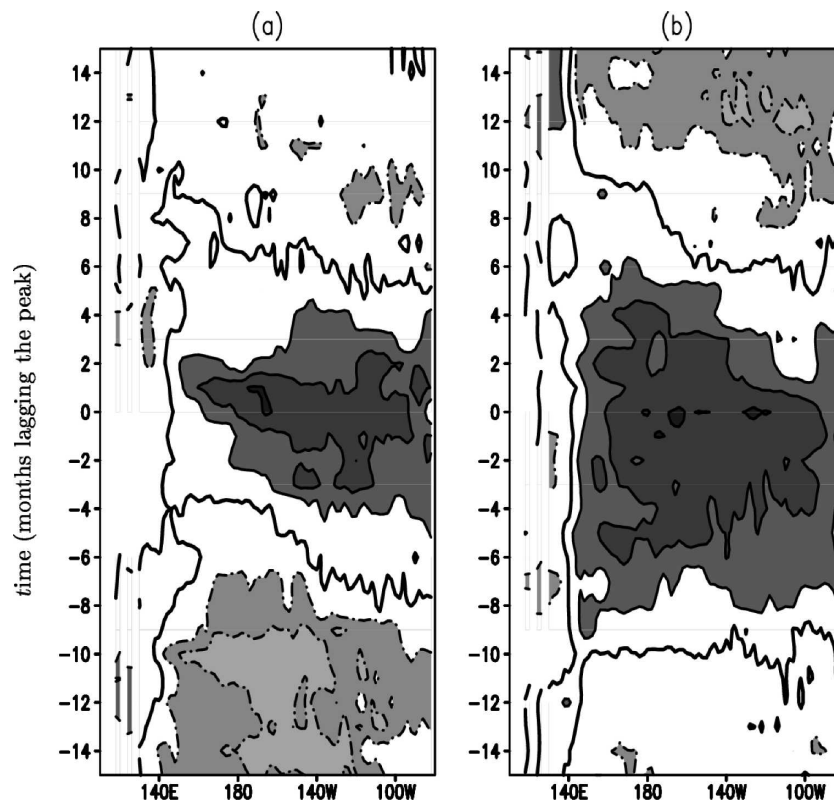

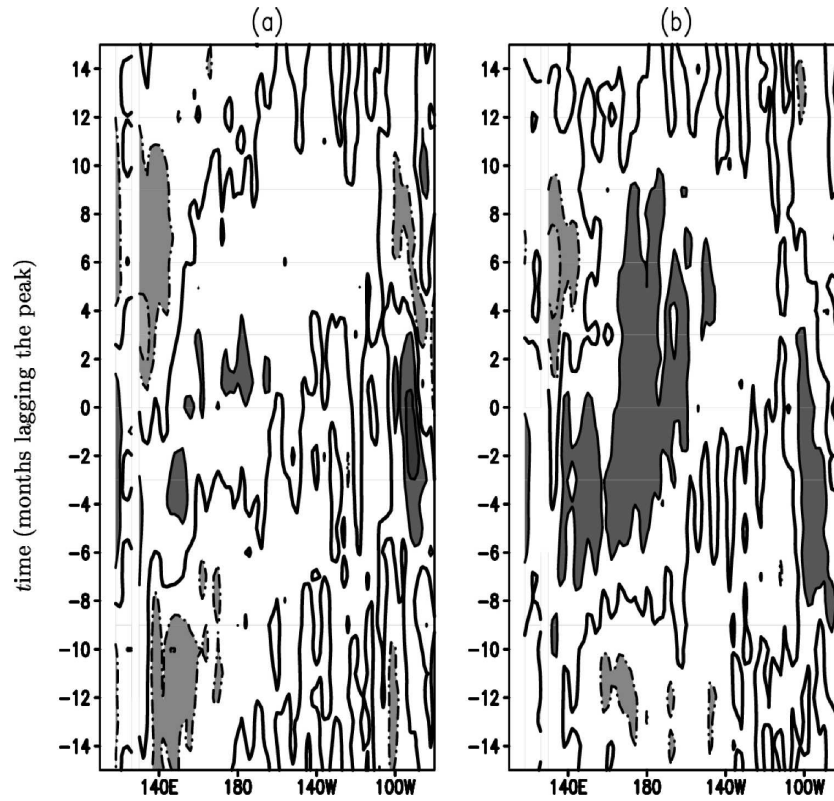FIG. 8. Same as in Fig. 7, but for normalized SST anomalies along the equator.

FIG. 9. Same as in Fig. 7, but for normalized 6-month-accumulated anomalies of meridional current across 1°N, averaged over 110–140 m.

in month 0 of composite W1, temperature anomalies (Fig. 13a) around 10°N appear unrelated to vertical velocity anomalies (Fig. 13b). They are rather connected with meridional current anomalies (Fig. 13c) through their advection of the meridional temperature gradient. However weak the latter is in the region, it might suf-

fice to yield significant SST anomalies in an area where the atmosphere becomes particularly sensitive to them, due to the mean wind convergence (Wang et al. 1999). We think this anomalous meridional advection might entwine SST and SLP in a positive feedback loop, as it may result from the equatorward winds (not shown) associated with the high SLP anomalies, which are in
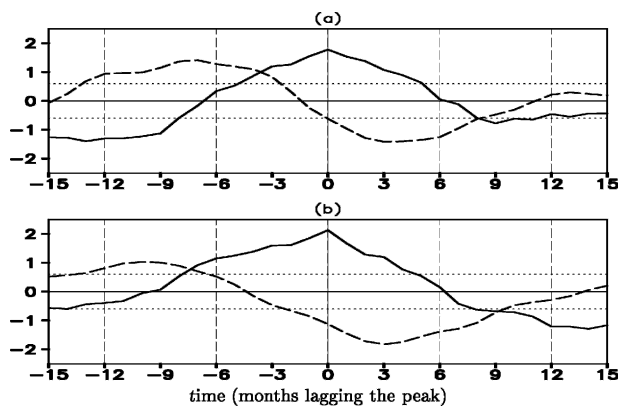

FIG. 10. Niño-3 normalized SST anomalies (solid line) and zonal mean thermocline depth normalized anomalies (dashed line): class (a) W1 and (b) W2. The horizontal dotted lines mark the 95% significance level.
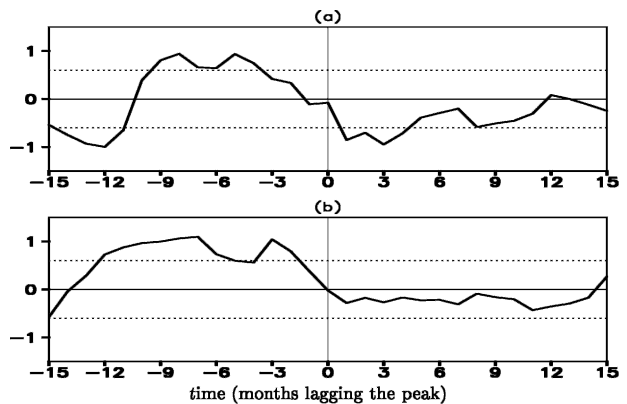

FIG. 11. Same as in Fig. 10, but for the Niño-5 normalized 3-month running mean zonal wind stress anomalies.
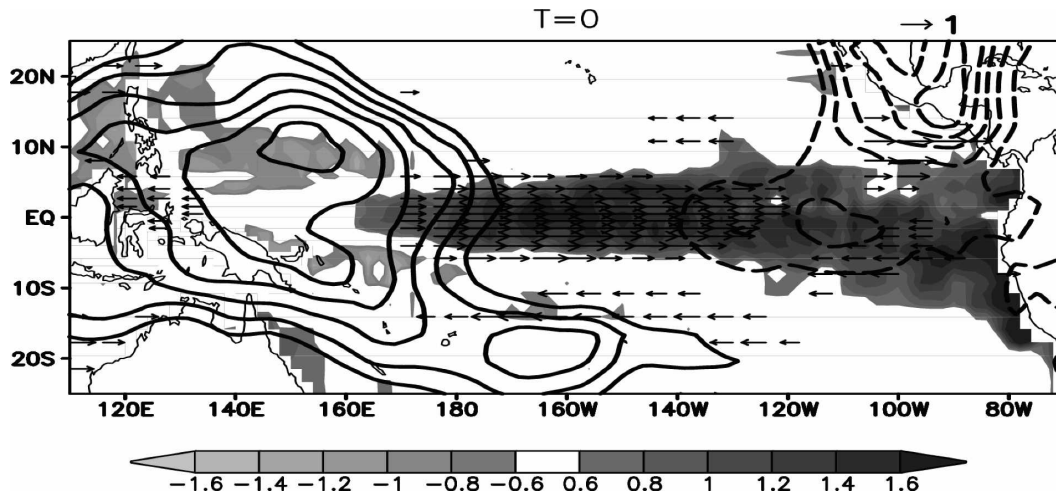
FIG. 12. Month 0 in composite W1. Contours: normalized SLP anomalies, showing absolute values above 0.6; contour interval is 0.2, solid (dashed) line denotes positive (negative) anomalies. Shaded: normalized SST anomalies. Arrows: normalized zonal wind stress anomalies.

turn sustained by the lower SST due to the advective anomalies.

c. The cold composite C1

Cold event–type C1 occurs as the aftermath to a previous warm event, which usually (six events out of nine in class C1) belongs to group W2. The onset of the cold episode in composite C1 represents the continuation of the panels in Fig. 6, as subsurface cold anomalies reach the eastern equatorial Pacific, approaching the surface in their travel from the west (not shown). In addition, anomalous zonal advection, due to anomalous zonal currents, also contributes to the sharp transition from the previous warm SST anomalies toward the current cold conditions (Fig. 14). Other advective terms (not shown) either fall below the significance threshold or are important only near the American coast. The timing and characteristic westward propagation of those zonal advection anomalies suggest they might be associated to equatorial (first meridional mode) Rossby waves arising from the reflection of Kelvin waves on the American coast during the warm episode and/or excited by easterly wind anomalies present over the eastern equatorial Pacific at that same time. The straight lines, labeled "Kelvin" and "Rossby," in Fig. 14, try to highlight this wave propagation. They are drawn assuming a phase speed of 2.8 m s^{-1} for the Kelvin wave and 1.0 m s^{-1} for the Rossby wave, the values estimated from observations by Delcroix et al. (1991) for the first baroclinic Kelvin and Rossby (first symmetric meridional mode) waves. These modes exert a strong influence on the evolution of observed ENSO variability (Picaut and Delcroix 1995; Delcroix et al.

2000). The zonal advection anomalies associated with this wave propagation, which carry equatorial SST anomalies from one phase to the opposite, play an important part in the advective–reflective oscillator paradigm of ENSO (Picaut et al. 1997).

The decay of the cold episode again features an active role of the northwest tropical Pacific in producing warm HC anomalies that eventually pass into the western equatorial Pacific. The evolution is reminiscent of that leading to the warm event in composite W1, but less clear. Only three out of nine events of type C1 are followed by a warm episode, which in all cases belongs to class W1.

d. Seasonal and decadal dependence of the classes

Early observations of ENSO already noticed a seasonal dependence in the generation and evolution of the warmings. Since 1980, some irregularities were detected (e.g., in the 1982–83 and 1992–93 events). Nevertheless the phase locking of the maximum of the anomalies to the boreal winter stands out as a regular feature of ENSO. It has been mentioned before that this is also a feature of a majority of the simulated events. Classes W1 and W2 are characterized by a rather realistic phase locking to the boreal autumn and winter (Fig. 15), with few exceptions, whereas no seasonal preference can be detected among the events of class W3 (the lack of seasonal locking is another reason to leave this last class of events out of our discussion in this work).

To investigate the connections of ENSO with decadal or interdecadal variability, we have filtered the HC anomalies so as to retain fluctuations with periods
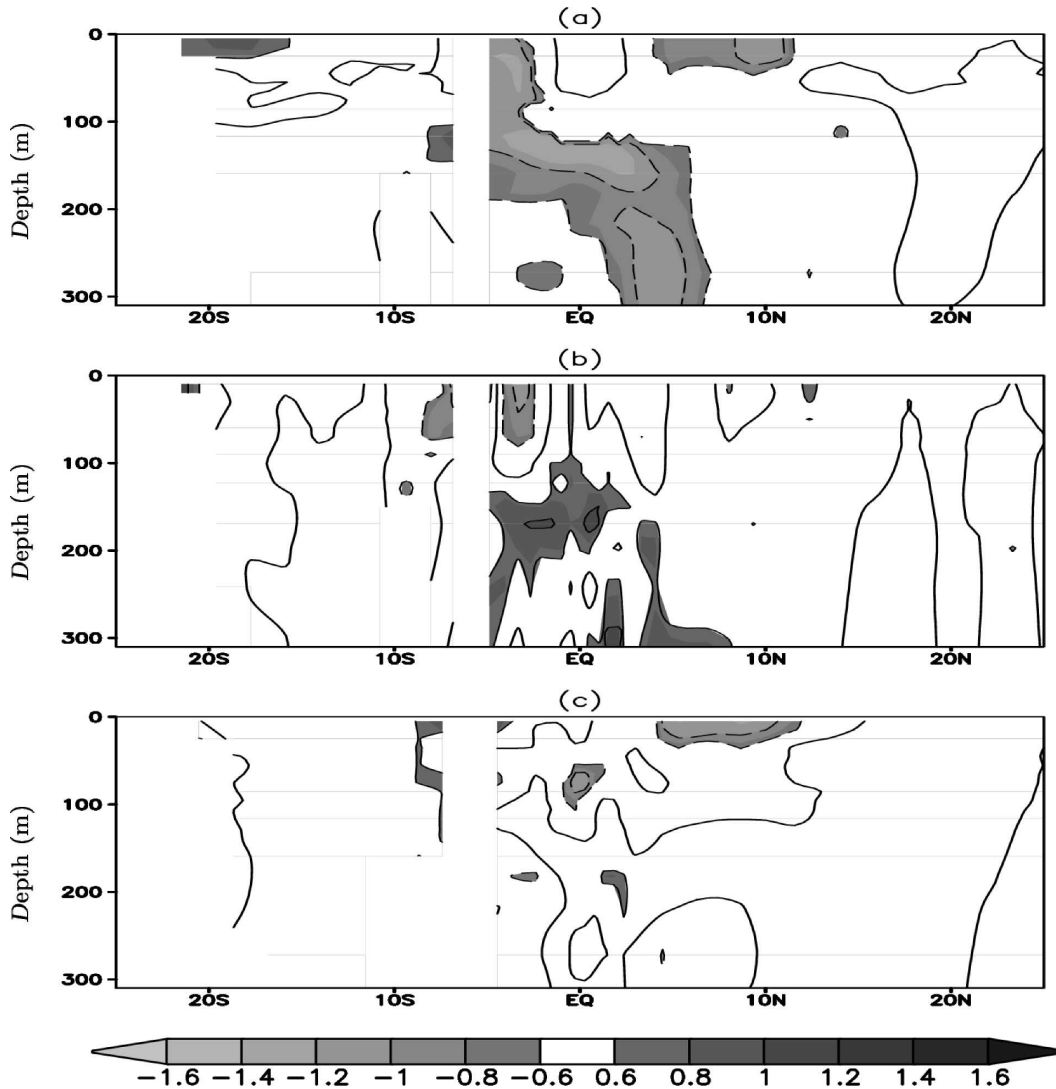
FIG. 13. Month 0 in composite W1: (a) depth–latitude section along 150°E of normalized temperature anomalies; (b) same as in (a), but for normalized 6-month-accumulated anomalies of vertical velocity; (c) same as in (a), but for normalized 6-month-accumulated anomalies of meridional velocity. Solid (dashed) line denotes positive (negative) anomalies.

above 8 yr. The time series depicted in Fig. 16 corresponds to the first principal component of the low-pass-filtered tropical Pacific HC anomalies. The change in the mean state of the last 50 yr is obvious. It is related with an intensification of the trades over the central equatorial Pacific and, subsequently, a steepening in the slope of the equatorial thermocline (not shown). There appears to be a link between this change and an additional feature of our classification: the uneven temporal distribution of the W2 events, which concentrate exclusively in the first half of the 100-yr record, as also shown in Fig. 16.

It was already stated that the effects of high-frequency processes on ENSO lie beyond the scope of

this work. No conclusions can be drawn on this issue with our approach here. We should mention, however, that significant patches of westerly zonal wind stress anomalies appear over the far western equatorial Pacific about 9 months ahead of the peak in the Niño-3 index, for both composites W1 and W2 (not shown). This would be consistent with frequent westerly wind bursts systematically preceding warm events and thus yielding a significant feature in the monthly composites. In nature, westerly wind bursts have often been associated with the MJO, whose propagating characteristics are not fully captured here. It would be then worthwhile to examine the relationship of the MJO and ENSO in SINTEX, both to ellucidate the role of west-
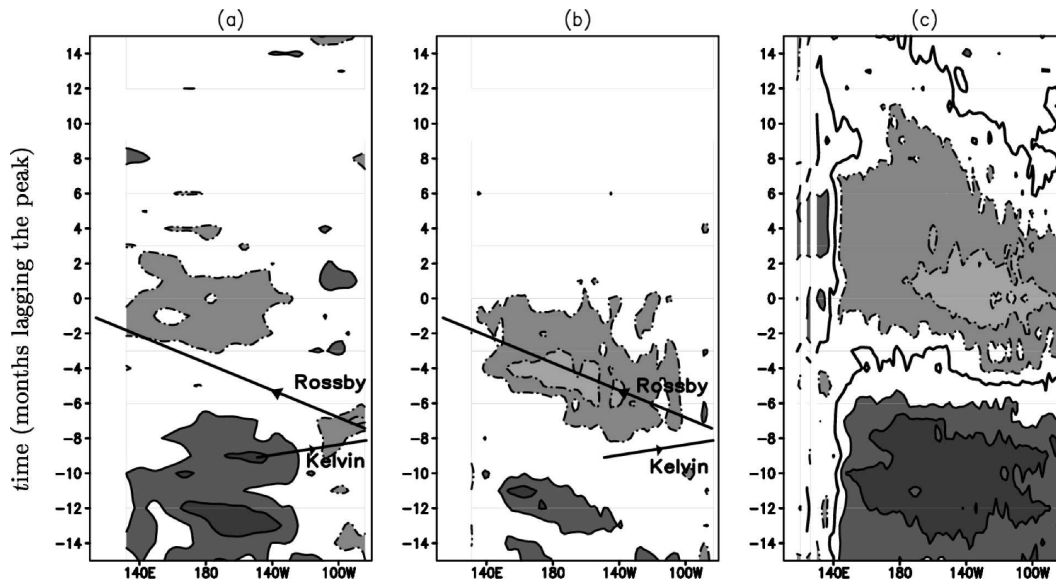
FIG. 14. Composite C1: equatorial time–longitude diagrams of (a) normalized zonal wind stress anomalies; (b) normalized zonal advection anomalies (due to anomalies in the zonal currents); contour interval in (a) and (b) is 0.4, only for absolute values above 0.6; solid (dashed) line for positive (negative) anomalies. (c) Normalized SST anomalies along the equator. Contour interval in (c) is 0.6, with zero or positive values in solid line. Absolute values over 0.6 are shaded.

erly wind bursts in the development of ENSO events and to determine how the errors in the modeled MJO, such as the tendency to produce standing rather than eastward-propagating oscillations and the limited penetration into the central Pacific, can affect the simulation of ENSO.

Finally, it should be noted that even if the wind stress anomalies might then be relevant for the development of warm events W1 and W2, some preconditioning of the ocean is still required, as suggested by the earlier presence of significant HC anomalies in both composites.

5. Summary and discussion

We present a classification of ENSO events occurring in 100 yr of a global simulation performed with the SINTEX CGCM. Warm episodes are grouped into three classes (W1, W2, and W3), and so are cold events (C1, C2, and C3). The paper is devoted to the analysis of ENSO generation and decay in the resultant composites, which characterize each class.

A first distinction arises as some composites (W3, C2, and C3) display a comparatively quick development, practically deprived of any significant anomaly until the event's peak is relatively near (less than 9 months ahead). Events of these types might illustrate "that given the right impetus, a weak warm event can occur

even without a substantial recharge of warm water in the upper layers of the equatorial Pacific" (Kessler 2002). Regarding such "right impetus," we can only conclude from our analyis that it is either too weak or lacks sufficient regularity to average any significant composite anomalies.

In agreement with the results of G03, accumulation of heat in the northwest tropical Pacific precedes the development of the warm episode in both composites W1 and W2 by several months. However, different mechanisms seem to be at work in each class: in situ growth in response to overlying WSC6 anomalies dominates in W2, as opposed to the westward propagation of HC and WSC6 anomalies characteristic of W1. This westward propagation is associated with significant cold phase anomalies in the eastern equatorial Pacific, which are basically absent in composite W2.

Furthermore, local reduction of heat content in the northwest tropical Pacific by WSC6 anomalies is again at work during the event's development in composite W2. Warm SST anomalies cover the equator at this stage, and the WSC6 anomalies over the northwest tropical Pacific consist with the atmospheric Gill-type response pointed out by G03. The shorter and less extended warm SST anomalies in composite W1 yield a set of atmospheric anomalies peculiar to the western Pacific oscillator at the peak stage.

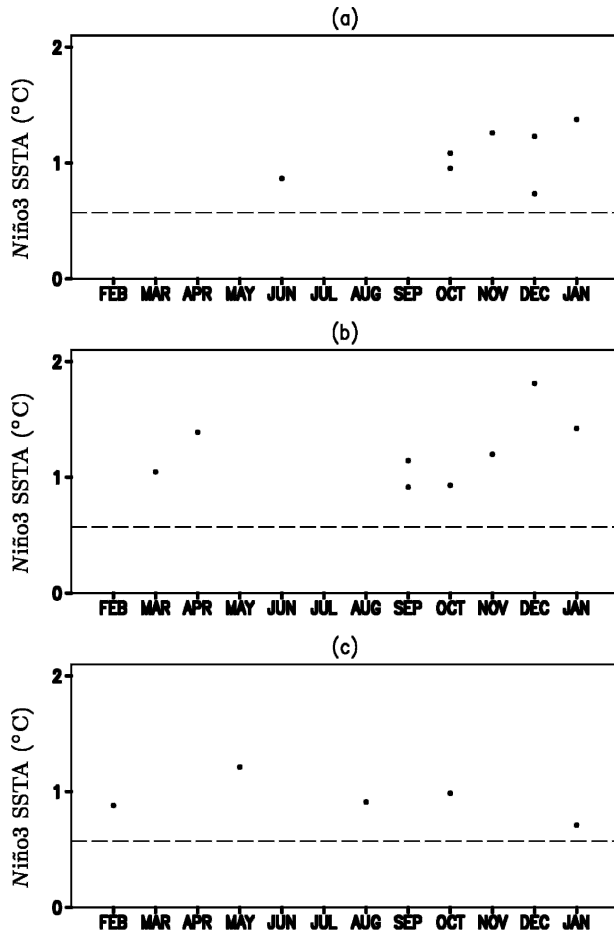Overall, composite W2 seems strongly reminiscent of

FIG. 15. Seasonal distribution of Niño-3 peaks for class (a) W1, (b) W2, and (c) W3. The *y*-axis units are in °C. The horizontal dashed lines mark the one standard deviation threshold.

the ENSO composite of G03. It must be stressed here that composite W1 is not likewise connected with G03's "aborted ENSO" composite. The latter is built on the basis of a vernal maximum in the Niño-3 anomalies,

whereas most of the elements within class W1 peak between October and December. Our classification technique apparently discriminates two distinct types of behavior that had been merged together by the use of an exclusively seasonal criterion in G03.

Among cold episodes, composite C1 alone presents significant preceding warm anomalies, corresponding to warm events of class W2. Equatorial zonal current anomalies seem to exert, through their impact in the advective regime, a major effect in rapidly changing the sign of the SST anomalies from warm to cold conditions, as is consistent with the postulates of the advective–reflective oscillator.

Transfer of subsurface cold anomalies from the west along the equatorial thermocline also participates in the generation of the cold event in composite C1. This kind of subsurface negative feedback—embodying the essence of the delayed oscillator paradigm—appears to act in all warm and cold composites, though not generally to carry the situation toward a new, opposite event. Globally, in fact, the oscillatory character of the simulated ENSO looks quite irregular, as already noted by G03. Our classification evidently does not depict a uniform sequence of warm and cold events.

The relationship with the seasonal cycle is relevant in the study of ENSO. Most ENSO composite analyses take it explicitly into account (the phase of the composite coincides with one season in the year). To have an objective classification and statistical significance at the same time, we gave up that approach in the present study. Nevertheless, it turns out that its application does not substantially modify our results, at least as far as classes W1 and W2 are concerned, given their realistic phase locking. This was checked in a complementary study performed with the fixed phase approach. The essential divission of classes and their characteristics hold under this perspective, though a few features of the composites lose significance.
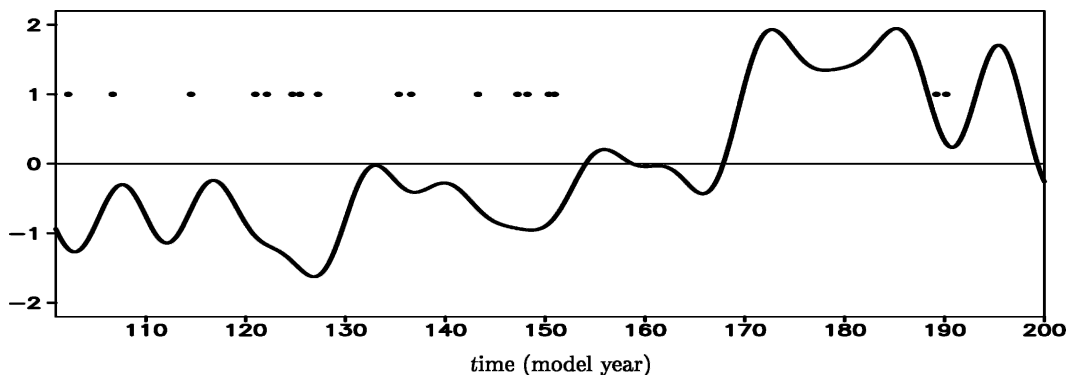

FIG. 16. First principal component of tropical Pacific decadal HC anomalies. Dots indicate the occurrence of W2–C1 events.

Interdecadal variability might explain the very existence of the classes W1 and W2 and its different physics. This point receives thorough attention in an upcoming paper, where the distinction between types W1 and W2 of warm events stands out as a consequence of both the interaction of interannual variability with the seasonal cycle and a regime shift in the middle of the record. As we mention at the beginning of this work, the sample size of the observations does not encourage this type of analysis. However, when tried on observed SST anomalies (1950–99), our procedure succeeds in detecting the change in ENSO behavior since the 1980s. Such change shares a number of features with the one occurring in the SINTEX simulation although, as pointed out by Harrison and Larkin (1998), it lacks statistical significance due to the limitations of the present observational record.

APPENDIX

Clustering Technique

Let p be one of the N ENSO episodes identified in the 100-yr record. Now let i range through the M grid points of the spatial domain under consideration (the tropical Pacific within 15°S and 15°N), and l take values from -15, denoting the time 15 months in advance of the peak of the event, to 0, that denotes the month when the peak occurs. Finally, let $h_i^p(l)$ denote the HC anomaly in the ith grid point of the domain and in time l of event p. To compare the evolution of these HC anomalies in episode p with the one of the HC anomalies $h_i^q(l)$ in some other episode q, we establish the following definitions of distance.

a. Distance

1) SPATIAL CORRELATION–BASED DISTANCE (D_1)

Spatial correlation between the HC patterns of events p and q at time l can be computed as

$$C^{pq}(l) = \frac{\sum_{i=1}^{M} h_i^p(l) h_i^q(l)}{\sqrt{\sum_{i=1}^{M} (h_i^p)^2 \sum_{i=1}^{M} (h_i^q)^2}}, \qquad \text{(A1)}$$

from which distance at time l can be given as

$$d_1^{pq}(l) = 1 - C^{pq}(l). \qquad \text{(A2)}$$

To obtain a single measure of distance, we average through the 16 values of l,

$$D_1^{pq} = \frac{1}{16} \sum_{l=-15}^{0} d_1^{pq}(l). \qquad \text{(A3)}$$

2) MEAN SQUARED DISTANCE (D_2)

An alternate definition of distance between p and q at time l is given by

$$d_2^{pq}(l) = \frac{\sum_{i=1}^{M} [h_i^p(l) - h_i^q(l)]^2}{\sqrt{\sum_{i=1}^{M} (h_i^p)^2 \sum_{i=1}^{M} (h_i^q)^2}}. \qquad \text{(A4)}$$

As before, we obtain a single value for each pair of events by averaging over l:

$$D_2^{pq} = \frac{1}{16} \sum_{l=-15}^{0} d_2^{pq}(l). \qquad \text{(A5)}$$

Applying each of these definitions, we compute distances for all possible (p, q) pairs. We establish an initial or seed classification by grouping events on the basis of a *shared near neighbors* criterion (Jarvis and Patrick 1973): a class is formed if at least three elements can be found with distances between any two of them below a fixed threshold. For the appearance of a second class, the additional restriction applies that its elements should be more distant to any of the first class than the said threshold. Once the classes are established, we characterize them by composites obtained as the average through their elements.

Next, we aim at enlarging the initial classes. We first compute the distance of unclassified episodes to the composites representing each group. The classes grow by gaining the events that are closest to them, given that distance lies below an *aggregation threshold.* Composites as well as these thresholds are updated after every entrance in a group. Eventually, classes will stop growing. The proximity of their elements to the class composite is checked. All elements within a class must be closer to the composite than a certain *final threshold.*
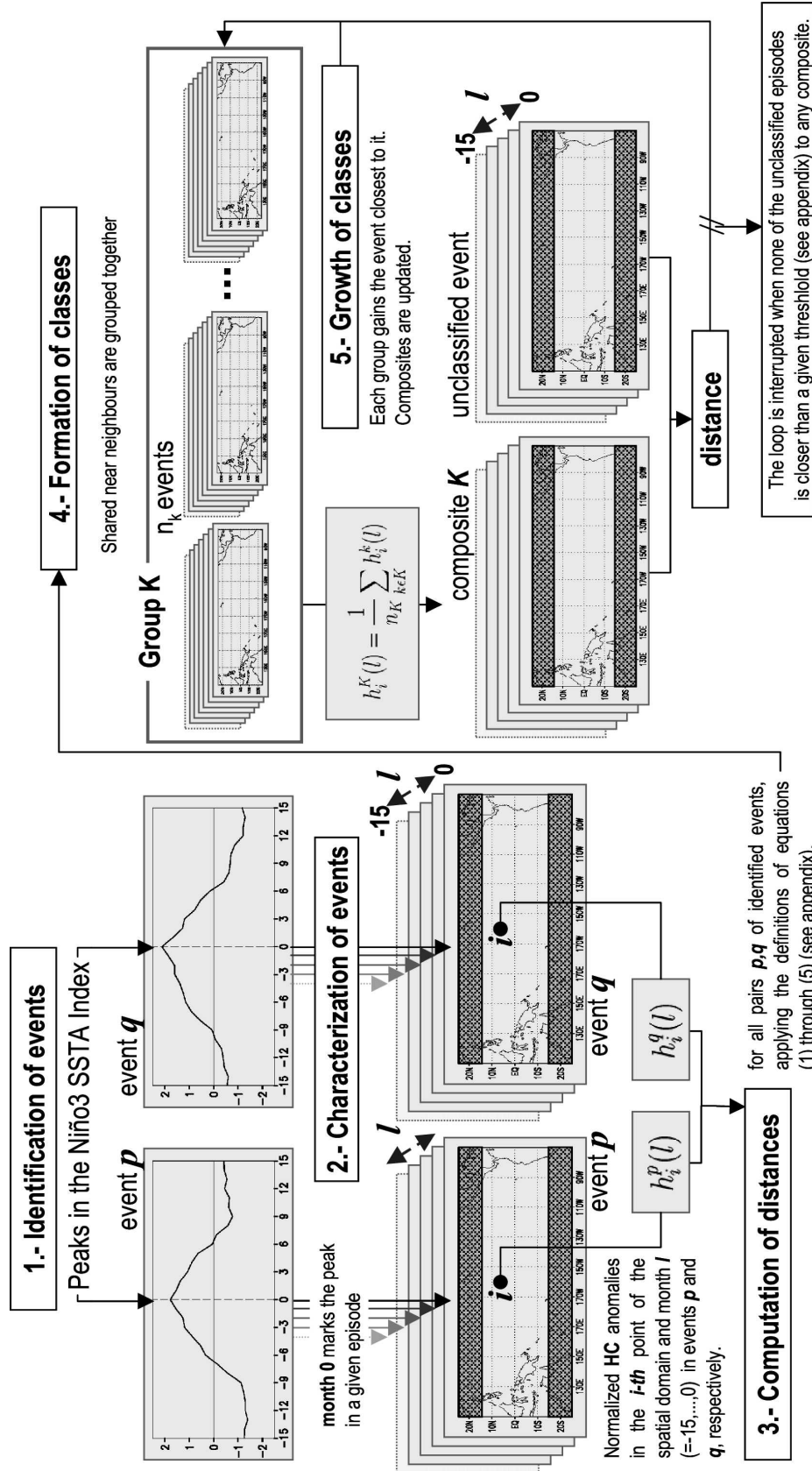
FIG. A1. Schematic diagram of the classification procedure.

Those that do not satisfy this condition are removed from the group.

The basic steps of the classification procedure are schematized in Fig. A1.

b. Aggregation and final thresholds

As previously detailed, we take each event to consist of 16 maps containing the tropical Pacific HC monthly anomalies leading to a peak in the Niño-3 series. For each of those months, one map can be picked at random from among the N available in our sample. The arrangement of 16 such random choices provides a synthetic episode. A large number of them can be derived from the original sample. The large, synthetically built sample is used to estimate the distribution of the distances to the group composites. We adopt an *aggregation threshold* for each class that is equal to the median of the proper distribution, whereas the fifth percentile is taken as the *final threshold.*

c. Robustness

The procedure explained above was followed separately for our two alternate definitions of distance. The comparison of the respective results revealed that the clustering is robust as regards the application of either measure of distance. The more relevant classes (W1, W2, and C1) are identical, but for the inclusion of one additional element in some cases. The final classes discussed in this work only include the common elements.

Last, we also tested the sensitivity of the clusters by removing individual events (one at a time, with replacement after each test) from the complete sample of 23 (19) warm (cold) episodes. We repeated the classification procedure on the different subsets of 22 (18) elements and checked whether similar groups were obtained. The results (not shown) largely confirmed the consistency of the initial classification.

REFERENCES

Battisti, D. S., and A. C. Hirst, 1989: Interannual variability in the tropical atmosphere-ocean system: Influences of the basic state, ocean geometry, and nonlinearity. *J. Atmos. Sci.,* **46,** 1687–1712.

Bjerknes, J., 1969: Atmospheric teleconnections from the equatorial Pacific. *Mon. Wea. Rev.,* **97,** 163–172.

Blanke, B., and P. Delecluse, 1993: Variability of the tropical Atlantic Ocean simulated by a general circulation model with two different mixed-layer physics. *J. Phys. Oceanogr.,* **23,** 1363–1388.

Boo, K.-O., G.-H. Lim, and K.-Y. Kim, 2004: On the low-level circulation over the western North Pacific in relation with the duration of El Niño. *Geophys. Res. Lett.,* **31,** L10202, doi:10.1029/2004GL019418.

Brown, T. J., and B. L. Hall, 1999: The use of *t* values in climatological composite analyses. *J. Climate,* **12,** 2941–2944.

Delcroix, T., J. Picaut, and G. Eldin, 1991: Equatorial Kelvin and Rossby waves evidenced in the Pacific Ocean through Geosat sea level and surface current anomalies. *J. Geophys. Res.,* **96,** 3249–3262.

——, B. Dewitte, Y. du Penhoat, F. Masia, and J. Picaut, 2000: Equatorial waves and warm pool displacements during the 1992–1998 El Niño–Southern Oscillation events: Observations and modeling. *J. Geophys. Res.,* **105,** 26 045–26 062.

Gualdi, S., A. Navarra, E. Guilyardi, and P. Delecluse, 2003: The SINTEX coupled GCM. The tropical Indo-Pacific region. *Ann. Geophys.,* **46,** 1–26.

Guilyardi, E., P. Delecluse, S. Gualdi, and A. Navarra, 2003: Mechanisms for ENSO phase change in a coupled GCM. *J. Climate,* **16,** 1141–1158.

Harrison, D. E., and N. K. Larkin, 1998: El Niño–Southern Oscillation sea surface temperature and wind anomalies, 1946–1993. *Rev. Geophys.,* **36,** 353–399.

Jarvis, R. A., and E. A. Patrick, 1973: Clustering using a similarity measure based on shared near neighbors. *IEEE Trans. Comput.,* **C22,** 1025–1034.

Jin, F.-F., 1997: An equatorial recharge paradigm for ENSO. Part I: Conceptual model. *J. Atmos. Sci.,* **54,** 811–829.

Kessler, W. S., 2002: Is ENSO a cycle or a series of events? *Geophys. Res. Lett.,* **29,** 2125–2128.

Latif, M., and Coauthors, 2001: ENSIP: The El Niño simulation intercomparison project. *Climate Dyn.,* **18,** 255–276.

Madec, G., P. Delecluse, M. Imbard, and C. Levy, 1998: OPA version 8.1 ocean general circulation model reference manual. Tech. Rep. LODYC/IPSL Note 11, 91 pp.

Mantua, N. J., and D. S. Battisti, 1994: Evidence for the delayed-oscillator mechanism for ENSO: The "observed" oceanic Kelvin mode in the far western Pacific. *J. Phys. Oceanogr.,* **24,** 691–699.

Mechoso, C. R., and Coauthors, 1995: The seasonal cycle over the tropical Pacific in coupled ocean–atmosphere general circulation models. *Mon. Wea. Rev.,* **123,** 2825–2838.

Meehl, G. A., P. R. Gent, J. M. Arblaster, B. L. Otto-Bliesner, E. C. Brady, and A. Craig, 2001: Factors that affect the amplitude of El Niño in global coupled models. *Climate Dyn.,* **17,** 515–527.

Neelin, J. D., D. S. Battisti, A. C. Hirst, F.-F. Jin, Y. Wakata, T. Yamagata, S. E. Zebiak, and D. Anderson, 1998: ENSO theory. *J. Geophys. Res.,* **103,** 14 261–14 290.

Picaut, J., and T. Delcroix, 1995: Equatorial wave sequence associated with warm pool displacement during the 1986–1989 El Niño and La Niña. *J. Geophys. Res.,* **100,** 18 398–18 408.

——, F. Masia, and Y. du Penhoat, 1997: An advective–reflective conceptual model for the oscillatory nature of the ENSO. *Science,* **277,** 663–666.

Rasmusson, E. M., and T. H. Carpenter, 1982: Variations in tropical sea surface temperature and surface wind fields associated with the Southern Oscillation/El Niño. *Mon. Wea. Rev.,* **110,** 354–384.

Rayner, N. A., D. E. Parker, P. Frich, E. B. Horton, C. K. Folland, and L. V. Alexander, 2000: SST and sea-ice fields for ERA40. *Proc. Second WCRP Int. Conf. on Reanalyses,* WCR 109 (WMO/TD-985), Wokefield Park, Reading, United Kingdom, WCRP, 18–21.

Röckner, E., and Coauthors, 1996: The atmospheric general circulation model ECHAM4: Model description and simulation

of present-day climate. Max Planck Institut für Meteorologie Rep. 218, 94 pp.

Sarmiento, J. L., and K. Bryan, 1982: An ocean transport model for the North Atlantic. *J. Geophys. Res.,* **87,** 394–408.

Sperber, K. R., J. M. Slingo, P. M. Innes, S. Gualdi, W. Li, P. J. Glecker, and C. Doutriaux, 2004: The Madden–Julian oscillation in GCMs. Preprints, *15th Symp. on Global Change and Climate Variations,* Seattle, WA, Amer. Meteor. Soc., CD-ROM, 4.10.

Suarez, M. J., and P. S. Schopf, 1988: A delayed action oscillator for ENSO. *J. Atmos. Sci.,* **45,** 3283–3287.

Terray, P., P. Delecluse, S. Labattu, and L. Terray, 2003: Sea surface temperature associations with the late Indian summer monsoon. *Climate Dyn.,* **21,** 593–618.

Valcke, S., L. Terray, and A. Piacentini, 2000: The OASIS coupled user guide version 2.4. Tech. Rep. TR/CMGC/00-10, CERFACS, 85 pp.

Wang, B., R. Wu, and R. Lukas, 1999: Roles of the western North

Pacific wind variation in thermocline adjustment and ENSO phase transition. *J. Meteor. Soc. Japan,* **77,** 1–16.

Wang, C., 2001: An unified oscillator model for the El Niño–Southern Oscillation. *J. Climate,* **14,** 98–115.

——, R. H. Weisberg, and J. Virmani, 1999: Western Pacific interannual variability associated with the El Niño–Southern Oscillation. *J. Geophys. Res.,* **104,** 5131–5149.

Weisberg, R. H., and C. Wang, 1997: A western Pacific oscillator paradigm for the El Niño–Southern Oscillation. *Geophys. Res. Lett.,* **24,** 779–782.

White, W. B., Y. M. Tourre, M. Barlow, and M. Dettinger, 2003: A delayed action oscillator shared by biennial, interannual, and decadal signals in the Pacific basin. *J. Geophys. Res.,* **108,** 3070, doi:10.1029/2002JC001490.

Yukimoto, S., and Y. Kitamura, 2003: An investigation of the irregularity of El Niño in a coupled GCM. *J. Meteor. Soc. Japan,* **81,** 599–622.